Al-Khwarizmi Engineering Journal

Al-Khwarizmi Engineering Journal
ISSN (printed): 1818–1171, ISSN (online): 2312–0789
Vol. 22, No. 3, September, (2026), pp. 75–88

Statistical Analysis of the Deposition Parameters of Multilayer AgO/Ag–TaO/TaO Thin Films on an SS316L Substrate

Mohd Amirul [1], Rodianah Alias [1,2]*, Muhammad Rizwan [3], W.N.F Mohamad [4], Abd Rahman Z. [5], M. S. Hamid [6], Afifah Juri [7], Mohd Faizal Ali Akhbar [8] and Abd Razak Bushroa [9]

[1,4,5,6] Faculty of Innovative Design and Technology, Universiti Sultan Zainal Abidin, Campus Gong Badak, 21300 Kuala Nerus, Terengganu Darul Iman, Malaysia
[1]Faculty of Information Sciences and Engineering, Management and Science University, University Drive, Off Persiaran Olahraga, Section 13, 40100 Shah Alam, Selangor, Malaysia
[2] Biomaterials & Nanomaterials Research Group, Smart Technology Cluster, Faculty of Innovative Design and Technology, Universiti Sultan Zainal Abidin, Campus Gong Badak, 21300 Kuala Nerus, Terengganu Darul Iman, Malaysia
[3] Department of Metallurgical Engineering, Faculty of Chemical and Process Engineering, NED University of Engineering and Technology, 75270, Karachi, Pakistan
[7] Department of Mechanical and Manufacturing Engineering, Faculty of Engineering and Built Environment, Universiti Kebangsaan Malaysia, 43600 Bangi, Selangor, Malaysia
[8] Department of Naval Architecture and Maritime Technology, Faculty of Ocean Engineering Technology, Universiti Malaysia Terengganu, 21030 Kuala Nerus, Terengganu, Malaysia
[9] Department of Mechanical Engineering, Faculty of Engineering, Universiti Malaya, 50603 Kuala Lumpur, Malaysia
* Corresponding author: rodianahalias@unisza.edu.my

(Received 27 August 2025; Revised 8 April 2026; Accepted 11 May 2026; Published 1 September 2026)
https://doi.org/10.22153/kej.2026.05.003

Abstract

Surgical instruments designed for high performance require coatings with strong mechanical properties, water-repellent features and compatibility with biological tissues to minimise interactions with bodily fluids during surgery. In this study, the structural and surface characteristics of multilayer AgO/Ag–TaO/TaO thin films deposited on a stainless steel 316L (SS316L) substrate by physical vapor deposition magnetron sputtering were investigated as functions of various deposition parameters. The effect of AgO deposition time and radiofrequency (RF) sputtering power was studied by using a central composite design with response surface methodology. Results demonstrate a significant correlation between the predicted and actual values of adhesion strength (R^2 = 0.9105), confirming the adequacy of the model. Adhesion strength was significantly affected by RF sputtering power then by deposition time. Wettability was also influenced by these parameters. Interaction plots show enhanced wettability at certain RF power levels, with a maximum contact angle of 89.6°. The optimal adhesion strength was obtained under specific RF power and deposition time conditions, with a maximum scratch distance of 705 mN. This work provides useful insights into the role of deposition parameters in tailoring the performance of thin films for biomedical and industrial applications.

Keywords: *Multilayer coating; deposition parameters; surface modification technology; adhesion strength*

1. Introduction

Biofilms consist of diverse microbial communities that attach to surfaces and generate a protective extracellular matrix, which enhances their resistance to antimicrobial treatments and host immune defences [1], [2]. They are the common causes of surface contamination in surgical and implantable instruments, leading to nosocomial and healthcare-associated infections [3], [4]. Approximately ~65%–80% of biofilm-related infections recur [5].

Importantly, antibacterial resistance and the emergence of chronic infections can result from the substantial influence of biofilms on immune responses and antibacterial efficacy [5]. Surgical instruments are indeed vulnerable to bacterial contamination with common pathogens, such as *Staphylococcus aureus*, *Pseudomonas aeruginosa*, *Escherichia coli* and *Candida auris* [6]–[10]. Therefore, the formation of surgical instrument–associated biofilms poses a challenge in healthcare.

Motivated by the development of surgical instruments with improved properties that overcome the adverse effects caused by coating detachment and bacterial attachment during surgical operations, we developed a multilayer AgO/Ag–TaO/TaO-based coating on the surface of a stainless steel 316L (SS316L) substrate under different deposition parameters for potential surgical instrument applications.

Incorporating thin films of Ag nanoparticles on SS316L implants is a common strategy employed in developing medical devices [11]. However, challenges remain, such as the poor adhesion strength of Ag on the SS316L substrate, limiting coating stability and causing delamination [12]. Numerous coatings for the surfaces of medical devices have been developed to enhance mechanical [13] and biological [14], [15] properties and thus minimise the risk of nosocomial infections. For example, various studies have been performed on the application of metal–composite coatings (commonly carbon nanotubes) on surgical instruments, an approach that has great potential to improve quality and efficiency [16]. Recently, Ta–W-based coatings deposited via physical vapor deposition (PVD) magnetron sputtering processes were utilised to enhance the surface properties of C_p–Ti (grade 2) substrates [17]. Although the coatings' hardness and antibacterial qualities were enhanced by the addition of Ag, corrosion performance was negatively influenced by the increase in gap count. For centuries, Ag has been recognised for its exceptional antimicrobial properties [18], [19]. It has been utilised in various medicinal forms because of its ability to inhibit the growth of a wide range of microorganisms [20]. Whilst the administration of a high concentration of Ag to open wounds might result in argyria [21], the use of Ag in biomedical applications is generally safe.

TaO is a promising and emerging biomaterial that exhibits cytocompatibility, antibacterial response and high blood compatibility [22] and can work synergistically with Ag's antimicrobial activity and biocompatibility. TaO is a good coating material for blood-contacting devices. such as SS316L, Ti-based stents and CrCo structures, because of its remarkable antithrombotic properties, particularly its strong resistance against blood coagulation [23]. Combining the promising properties of the abovementioned coating materials could lead to the development of advanced coatings with desirable characteristics, thereby enhancing people's quality of life.

Advances in the development of single or multilayer Ag- and TaO-based coatings for surgical instruments [24], [25], medical implants [15], [26] and biomaterial devices [27], [28] deposited via PVD magnetron sputtering are on the rise. For example, Ag–Ta_2O_5-based coatings for surgical instruments exhibit good adhesion strength, biocompatibility and antibacterial response [24], [29]. The addition of an excess 12.5 at.% Ag to Ta_2O_5 and Ta_2O_5–Ag coatings on an SS304 substrate enhanced antibacterial effect and cytocompatibility [27]. For applications in implants, Ta and TaO coatings on SS316L demonstrate noncytotoxicity [30]. TaO is a suitable binding agent for Ag because of its exceptional adhesion strength on SS316L [24]. These results highlight the importance of selecting the appropriate materials for thin-film coatings to ensure strong adhesion and durability, particularly in biomedical applications where biocompatibility is crucial.

The PVD magnetron sputtering technique offers various advantages, including high material deposition rates, good surface morphology and low substrate temperatures, and has been widely employed for depositing diverse thin-film coatings [31], [32]. Numerous parameters are involved in deposition. They include gas flow rate [33], direct current (DC)/radiofrequency (RF) sputtering power [34], [35], sputtering pressure [36] and substrate temperature. The application of mathematical models in the analysis of the deposition parameters of multilayer AgO/Ag–TaO/TaO is rarely studied but could provide insights into the optimal combination of deposition conditions for producing quality coatings with improved properties.

In this study, we investigate a new approach for evaluating the influence of deposition time and RF sputtering power on multilayer AgO/Ag–TaO/TaO coatings on an SS316L substrate. We systematically studied the effects of deposition time and RF sputtering power on the adhesion strength and hydrophobicity of multilayer AgO/Ag–TaO/TaO coatings on SS316L. Our model demonstrated high predictive accuracy and resulted in improvements in adhesion and wettability, suggesting its potential to enhance the performance and biocompatibility of coating technology for surgical instruments.

2. Methodology

2.1. Specimen Preparation

Commercial Ta and Ag with purities of 99.95% and 99.99%, respectively, produced by China Rare Metal Materials Co. Ltd were employed as target materials. A total of 13 SS316L sheets, each with dimensions of 5 mm × 10 mm × 5 mm, were used as substrates. Polishing was performed with 6 and 1 µm polycrystalline diamond suspensions to obtain surfaces with a mirror finish. Afterwards, samples were rinsed with distilled water, air-dried and then ultrasonically cleaned in acetone and ethanol for 15 min before being dried again at room temperature.

2.2. Analysis of Variance

The central composite design in response surface methodology was applied, and statistical analysis was carried out with Design Expert software by using analysis of variance (ANOVA). The conditions and levels applied for AgO/Ag–TaO/TaO deposition are given in Table 1. Table 2 shows the design matrix layout. The first two columns in the table list the primary input factors, with each set at various levels, whereas the remaining columns show the scratch distance and contact angle values. In this study, ANOVA was conducted to assess the significance of factor effects, and interactions between the main effects were examined. The interaction plot provides a clear view of the influences and interactions amongst variables, enhancing understanding.

Table 1,
Input variables with their corresponding levels as the process parameters.

Factors	Units	Min	Max
Ag deposition time for the second layer	Minutes	20	40
RF power for the Ag target in the second layer	Watts	100	200

2.3. PVD Magnetron Sputtering Deposition

Multilayer AgO/Ag–TaO/TaO thin films were deposited by using a PVD magnetron sputtering system (Model TF450, SG Control Engineering, Singapore), as illustrated in the schematic in Figure 1. Each sample to be deposited was inserted and well placed in the deposition chamber, as depicted in Figure 2. A series of 13 experiments was performed under different Ag deposition times and RF sputtering powers for the first AgO layer, whereas the DC power voltage for the Ta target and substrate temperature were kept constant at 200 W and ~100 °C, respectively. The values of the deposition parameters for the first AgO layer and the average (obtained through triplicate reading) adhesion strength and contact angle values of the as-sputtered coatings are listed in Table 2.

For the second Ag–TaO thin layer, the deposition time was set to 20, 30 and 40 min. The chamber's base pressure was evacuated to approximately 2.67×10^{-3} Pa. The target surfaces were presputtered in Ar gas before deposition to minimise contamination within the vacuum chamber. The process pressure and gas flow were controlled by using the control panel of the PVD system, as shown in Figure 3. The target-to-substrate distance was maintained at 15 cm, and no bias voltage was applied to the substrate. Once the deposition procedure of each sample was completed, the sample was removed from the PVD chamber and kept in a dry box for subsequent characterisation.

Table 2,
Layout of the design matrix.

Run	Fac 1: AgDt (Min)	Fac 2: RFP (W)	SD (µm)	CA (°)	CT (µm)
1	20.0	100.0	392.7	84.2	2.13
2	40.0	100.0	605.3	77.9	2.01
3	20.0	200.0	574.3	89.6	2.00
4	40.0	200.0	634.0	69.1	3.13
5	15.9	150.0	429.3	80.2	2.5
6	44.1	150.0	565.0	80.8	1.07
7	30.0	79.3	326.3	84.2	2.29
8	30.0	220.7	391.3	82.0	2.91
9	30.0	150.0	468.0	82.0	2.53
10	30.0	150.0	520.6	79.5	1.94
11	30.0	150.0	454.0	86.2	2.5

12	30.0	150.0	529.6	80.6	1.94
13	30.0	150.0	511.6	80.0	1.64

Note* AgDt: Ag Deposition time. RFP: RF Power. SD: Scratch Distance. CA: Contact Angle. CT: Coating Thickness. Fac: Factor.

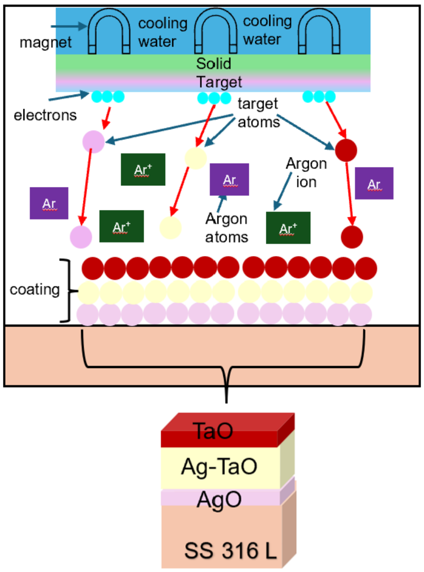

Fig. 1. Schematic of PVD sputtering and the multilayer AgO/Ag–TaO/TaO coating deposited on SS316L.

2.4 Adhesion Strength and Wettability Characterisations

The adhesion strength between the coating and substrate was evaluated by using a microscratch testing system (Micro Materials Ltd., Wrexham, the UK). Stability and durability over time are important key features of surgical instruments. Moreover, surgical instruments should not easily chip or release particles when in use. A strongly adhering antibacterial coating layer can improve efficiency by reducing contamination and infection risks [13]. The adhesion strength between the coating and substrate was evaluated on the basis of the scratch distance and critical load values Lc_1, Lc_2 and Lc_3 taken from the load–displacement curve. The critical load (Lc) was determined from the frictional response curves and microscopic analysis of scratch tracks [12].

The test began by using a diamond tip to apply an initial load of 0 mN on the sample. The load then increased to 1500–3500 mN with a sliding speed of 6.0 µm/s and over a track length of 1000 µm. The critical loads Lc_1, Lc_2 and Lc_3 were obtained from the load–displacement graphs based on the scratch profiles generated by testing each sample in a left-to-right direction [37].

Figure 4 illustrates the critical load points: Lc_1 corresponds to cohesive failure, with side scratches and minor tensile cracking along the scratch. Lc_2 indicates delamination along the trackside. Further delamination and cracking are observed under increasing loads until reaching Lc_3, when the thin film completely detaches from the substrate along the scratch track.

As the applied load increased, delamination developed around the track edges, indicating Lc_2. When the load increased further, cracking and delamination aggravated, and the coating ultimately detached completely from the substrate, a phenomenon corresponding to Lc_3 [33]–[39].

Fig. 2. Vacuum deposition chamber

Fig. 3. Control panel of the PVD magnetron sputtering system

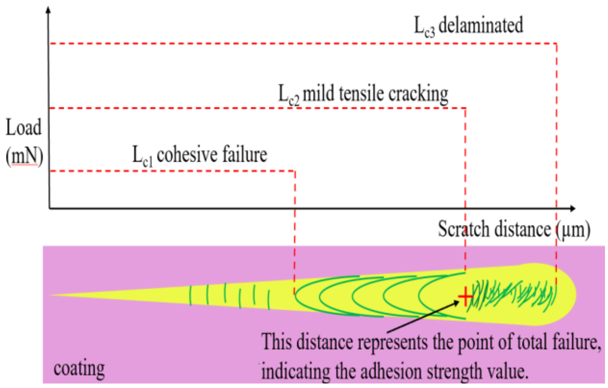

Fig. 4. Schematic illustration of the determination of Lc_1, Lc_2 and Lc_3 to assess adhesion strength.

Contact angle measurements were performed by using an optical system (OCA 15EC; DataPhysics Instruments GmbH, Germany) with distilled water as the test liquid to assess the hydrophobic nature of the AgO/Ag–TaO/TaO coating. Droplet size and dispensing rate were controlled at 3 µL and 2 µL/s, respectively. A hydrophobic surface is particularly beneficial for surgical tools because it enables a water-repellent surface, which helps prevent the attachment of blood, fats and other bodily fluids to the instruments. Such a feature improves the surgeon's field of view, reduces blood loss and keeps instruments clean throughout the operation; extends lifespan; and, importantly, prevents bacterial adhesion [40]. Hydrophilic surfaces exhibit low contact angles because they retain fluid [12].

A surface's wettability and contact angle help determine its physical characteristics and surface energy. In accordance with Young's equation (1), the equilibrium contact angle θ_0 for a droplet on a flat surface can be expressed as [12]

$$\theta = \frac{\gamma LV - \gamma SL}{\gamma LV} \quad ...(1)$$

In this context, γ_{SV}, γ_{SL} and γ_{LV} denote the interfacial tensions per unit length at the solid–vapour, solid–liquid and liquid–vapour interfaces, respectively, as illustrated in Figure 5. The sessile drop technique was employed to evaluate surface wettability by measuring the contact angle at the point where a distilled water droplet contacts the specimen, corresponding to the intersection of the liquid–vapour (γ_{LV}) and solid–liquid interfaces (γ_{SV}), as depicted in Figure 5.

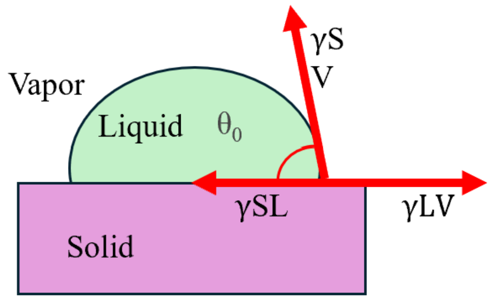

Fig. 5. Schematic illustration of the wettability study based on the contact angle of ultrapure double-distilled water

2.5 Surface Microstructural, Topography, Elemental and Phase Analyses

Microstructural and elemental analyses were performed on the coatings by using field-emission scanning electron microscopy (Thermo Fisher Scientific Quattro ESEM, the USA) and energy-dispersive X-ray spectrometry. Furthermore, extended surface topography was measured in noncontact mode by using an atomic force microscope (PARK NX 10, Korea). Phase identification was performed with an X-ray diffractometer (XRD, PANalytical Empyrean, the Netherlands) using Cu–Kα radiation. The operating voltage and current were set at 40 kV and 40 mA, respectively, over a 2θ range of 10°–90°.

2.6 Coating Thickness Evaluation

Coating thickness (CT) was determined by analysing the vertical displacement (Δd) from the initial surface baseline to the stable plateau recorded after the indenter fully penetrated the coating and reached the substrate interface. This transition from the coating surface to the substrate plateau serves as the proxy for total thickness, as detailed in Figure 6.

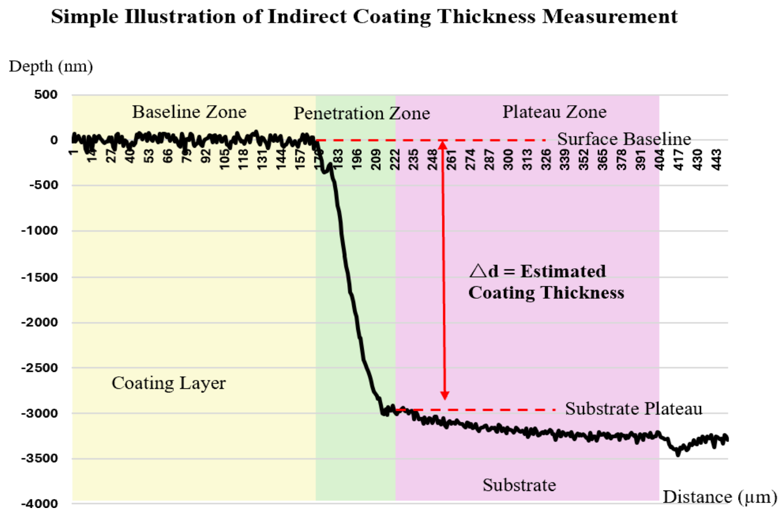

Fig. 6. Indirect coating thickness measurement via scratch profiling. The penetration depth △d from the surface baseline to the substrate plateau provides the total thickness estimate.

3. Results and Discussion

3.1 ANOVA of Adhesion Strength

After we estimated the scratch distance, we determined its interacting factors by analysing variance through ANOVA. The results were analysed by using Design Expert software. The fit summary output shows that without transforming the response, the linear model exhibited statistical significance for both responses. Therefore, we adopted this model for further evaluation. Table 3 shows that the main and interaction effects of each factor with $P < 0.05$ were considered potentially significant.

3.2 Regression Analysis of Scratch Distance

We developed a mathematical model by using ANOVA to determine how Ag deposition time and RF power significantly influence the scratch distance of the AgO/Ag–TaO/TaO coating. In the final equation, actual factors can be used to predict the response for each factor at a given level. The prediction equation for scratch distance and contact angle is

Scratch distance (µm) = +75.62574 + 3.60846 × D time (min) + 2.09851 × RF power (W) Ra.

3.3 Interaction Plot of Scratch Distance

We investigated the effects of deposition time on scratch distance in a system maintained at a constant RF energy level, with an actual factor value of 150. Adhesive strength is a critical property of bonded materials and is particularly crucial in RF-assisted curing processes where time and energy are integral to achieving high-performance bonds.

Design Expert generated a one-factor plot that showed the proportional relationship between deposition time and scratch distance within the examined range (Figure 7). Increased deposition time is associated with an extended scratch distance, consistent with the hypothesis that increasing deposition time results in complete curing because cross-linking in the adhesive matrix is enhanced at the molecular level, leading to strengthened interfacial bonding between substrates.

We also employed Design Expert to generate a one-factor plot that illustrates a proportional relationship between Ag RF power and adhesive strength within the experimental range (Figure 8). Adhesive strength also increased with increasing RF power, suggesting that high RF energy input promotes improved adhesion, indicating that additional energy is available for complete curing and cross-linking accelerated within the adhesive structure, an effect that may enhance molecular cohesion and strengthen the bonds at material interfaces. This result demonstrates that RF power is a significant parameter for adhesive strength and that under the fixed deposition time of 30, increasing RF power levels can have a positive effect on the quality of bonds.

3.4 ANOVA of Contact Angle

We subjected the results of contact angle analysis to ANOVA to identify the interacting factors influencing contact angle. The obtained results were processed by using Design Expert software. The fit summary output, evaluated without response transformation, demonstrated that the linear model was statistically significant for both responses.

Therefore, this model was employed for further interpretation, as shown in Table 4. Factors with main and interaction effects with $P < 0.05$ were considered potentially significant.

Table 3,
ANOVA results for the linear model of scratch distance. The table highlights the significance of factors A and B and includes the lack-of-fit test and model fit statistics.

Source	Sum of Squares	DF	Mean Square	F Value	Prob > F	
Model	71158.51	2	35579.25	40.68	<0.0001	Significant
A	8754.36	1	8754.36	10.01	0.0133	
B	53399.27	1	53399.27	61.06	<0.0001	
Residual	6996.62	8	874.58			
Lack of Fit	2464.49	4	616.12	0.54	0.7152	
Pure Error	4532.13	4				

Std. Dev. = 29.57. **R-Squared = 0.9105**. Mean = 491.42. Adj R-Squared = 0.8881.
Pred R-Squared = 0.8406.

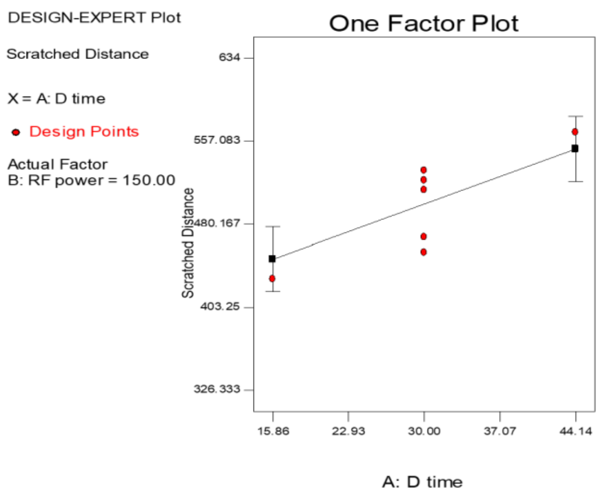

Fig. 7. One-factor plot (Ag deposition time versus adhesive strength across the examined range).

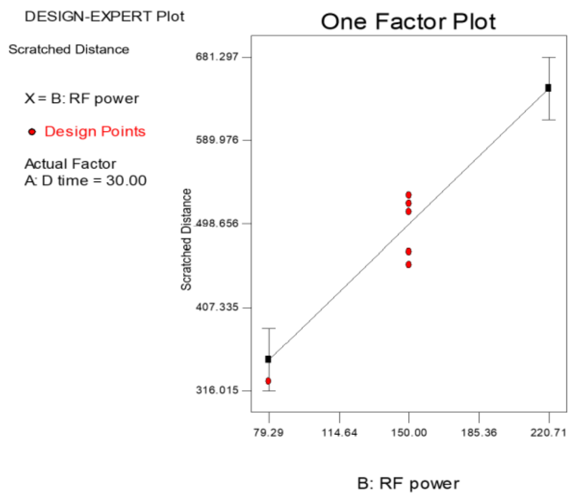

Fig. 8. One-factor plot (Ag RF power versus adhesive strength within the experimental range).

3.5 Regression Analysis of Contact Angle

We established a mathematical model by using ANOVA to estimate the significant effects of Ag deposition time and RF power on the adhesion strength of the AgO/Ag–TaO/TaO coating. In the resulting equation, actual factors can be used to predict the response of each factor at specific levels. The predictive equations for adhesion strength and contact angle are presented as

$$\text{Contact angle } (^\circ) = +46.81305 + 2.77471 \times \text{D time (min)} + 0.044317 \times \text{RF power (W)} - 0.038317 \times \text{D time}^2\ (\text{min}^2) + 5.09618\text{E}{-}004 \times \text{RF power}^2\ (\text{W}^2) - 7.11500\text{E}{-}03 \times \text{D time (min)} \times \text{RF power (W)}.$$

3.6. Interaction Plot of Contact Angle

The interaction plot generated by Design Expert indicates that contact angle exhibited distinct behaviours under minimum and maximum RF power conditions. At the minimum RF power level (79.289), an increase in deposition time initially enhanced contact angle, which peaked at a time value of 30 (Figure 9). Beyond this peak, further increasing deposition time led to a decline in contact angle, indicating an optimal time threshold at low RF power levels. On the other hand, at the maximum RF power level (220.711), contact angle rose as deposition time fell, suggesting that time and contact angle have an inverse relationship under high power settings. This inverse trend may reflect accelerated surface energy modifications or structural changes induced by high energy input over short durations, thereby rapidly increasing contact angle. The nonlinear interaction graph curve is supported by statistical analysis, with a P-value of 0.0269 for the A^2 term, indicating that this term is the most precise for this data. The AB term (P = 0.0388) shows the differences in slope between the two lines, demonstrating that the effect of deposition time depends strongly on RF power. The declining pattern under elevated deposition times demonstrates a saturation point at which RF energy can increase hydrophilic properties.

Table 4,
ANOVA results for the quadratic model of contact angle. The analysis identifies the significance of main effects (A), quadratic effects (A^2) and interaction effects (AB) alongside model fit statistics (R^2 and Adj R^2) and the lack-of-fit test results.

Source	Sum of Squares	DF	Mean Square	F Value	Prob > F	
Model	233.87	5	46.77	6.41	0.0213	Significant
A	167.96	1	167.96	23.03	0.0030	
B	5.28	1	5.28	0.72	0.4275	
A2	61.82	1	61.82	8.48	0.0269	
B2	10.53	1	10.53	1.44	0.2748	
AB	50.62	1	50.62	6.94	0.0388	
Residual	43.75	6	7.29			
Lack of Fit	14.51	2	7.26	0.99	0.4466	
Pure Error	29.24	4				

Std. Dev. = 2.70. **R-Squared = 0.8424**. Mean = 81.30. Adj R-Squared = 0.7111. Pred R-Squared = 0.3691.

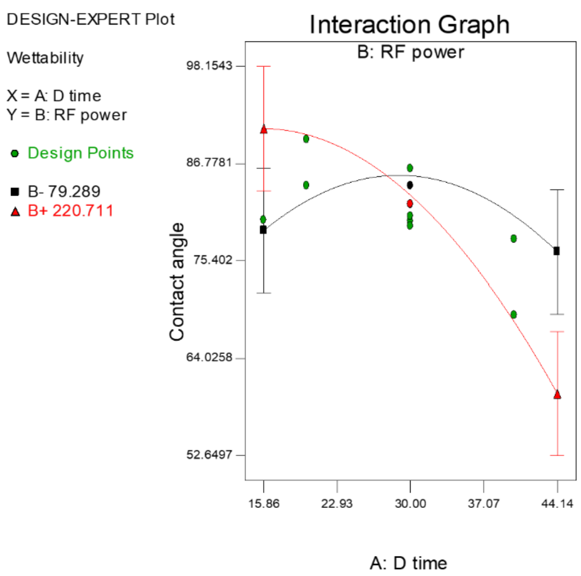

Fig. 9. Interaction plot illustrating the distinct behaviours of contact angle under minimum and maximum RF power conditions.

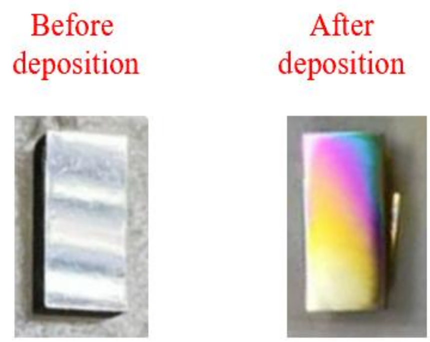

Fig. 10. Sample surface before and after deposition.

3.7. Visual Appearance, Adhesion Strength and Wettability Characterisations

Figure 10 shows that the sample surface initially appeared shiny silver then became iridescent after deposition.

Figure 11 displays the adhesion strength analysis graphs, showing depth and load versus distance, alongside images of contact angles. Table 2 shows that the Run 4 and 7 samples exhibited the maximum and minimum scratch distance values, respectively. We determined the values of adhesion strength by analysing the scratch distance and critical load values (Lc_1, Lc_2 and Lc_3) extracted from the load–displacement graph. As seen in the uppermost part of Figure 8, the failure point in the Run 4 sample was detected at a distance of 634 µm. At this distance point, the coating withstood an applied load of 705 mN before failure. This result indicates that the adhesion strength of the Run 4 sample is 705 mN. In the Run 7 sample, the failure point occurred at 326 µm, with the coating sustaining an adhesion strength of approximately 304 mN.

By contrast, the Run 3 and 4 samples recorded the highest and lowest contact angle measurements, respectively. As shown in the bottom part of Figure 11, the contact angles of the Run 3 and 4 samples were 89.6° and 69.1°, respectively. The Run 3 sample had the highest hydrophobicity amongst samples but did not have the highest adhesion strength. As reported above, the Run 4 sample, which showed the highest adhesion amongst samples, had the lowest hydrophobicity. Our study proves that wettability properties indirectly determine adhesion strength. Similar phenomena have been reported in several previous studies [41]–[43]. This finding suggests that the Run 3 and 4 samples exhibit wettability and adhesion strength favourable for applications in surgical instruments.

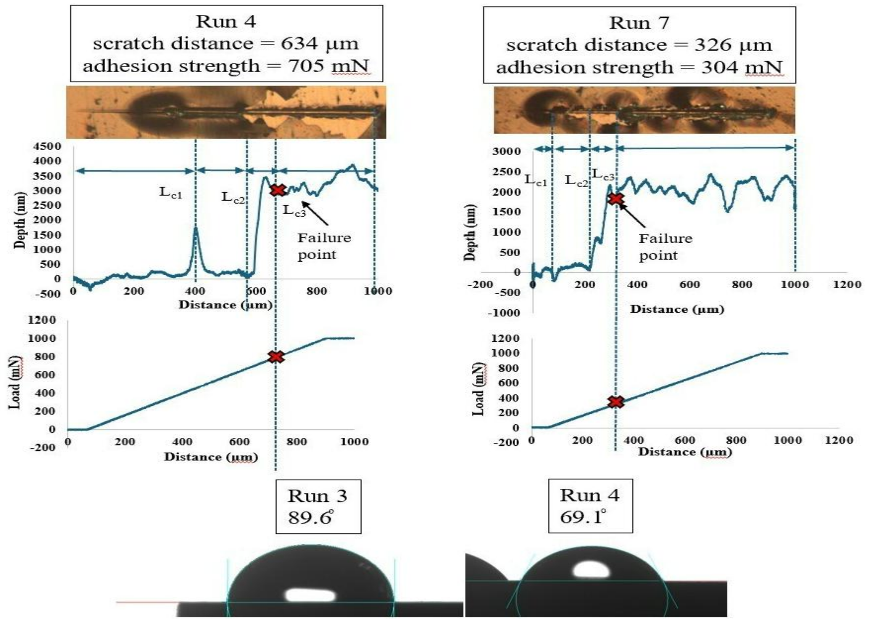

Fig. 11. Optical surface scratch images; depth and load with respect to the scratch distance graph; failure points of the Run 4 and 7 samples (top part); and contact angles (bottom part) of the Run 3 and 4 samples.

3.8. Surface Microstructural, Topography and Elemental Analyses

The image on the left side of Figure 12 presents the surface microstructures of the Run 4 and 7 samples. Particles in the Run 4 sample exhibited a uniform and dense distribution. The microstructure of the Run 7 sample displayed a cauliflower-like pattern with discrete spherical coating particles. The Run 4 sample, which was processed under a higher RF power and longer deposition time than the Run 7 sample, not only demonstrated dense and uniform morphology but also showed the highest adhesion strength, as depicted in Figure 11. The dense, compact distribution of coating particles reduces the number of voids through mechanical interlocking. This finding is in line with that reported by Zhu et al. [44]. The elemental analysis result in the upper right side of Figure 12 confirmed that the AgO/Ag–TaO/TaO coating was deposited on the Run 4 sample. Cross-sectional analysis for evaluating multilayer thickness and composition is scheduled for subsequent work. Given that the Run 4 sample showed the best mechanical performance amongst all samples, we examined its surface topography.

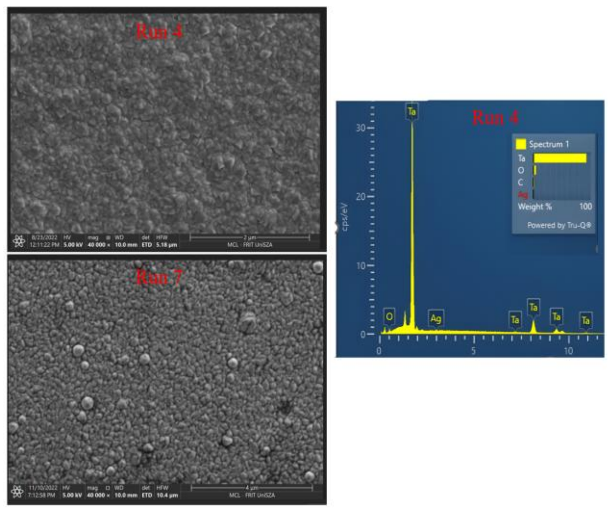

Fig. 12. Surface microstructures of the Run 4 and 7 samples and elemental analysis of the Run 4 sample.

The AFM 3D view of the Run 4 sample in Figure 13 displays homogenously distributed AgO/Ag–TaO/TaO coatings with a root mean square roughness (Rq) of 0.0194 μm. The white mountainlike topography seen in this figure is correlated with a feature in the microstructure image in Figure 14. The Run 4 and 7 samples showed similar trends: Ta_2O (98-002-8387), Ag (98-004-4387) and Ag_2O (98-002-0368) were present on the surfaces of both samples. Ta_2O appeared at the 2θ positions of 38.07, 58.58, 68.80 and 81.43 corresponding to the orientations of the cubic crystal

planes (0 2 2), (1 1 4), (2 2 4) and (0 4 4), respectively. Ag peaks appeared at the 2θ positions of 38.12 and 44.31 at (1 1 1) and (2 0 0), respectively. Ag_2O diffraction peaks were observed at 33.59, corresponding to the (1 0 0) plane. No additional diffraction peaks related to secondary phases were observed in the XRD patterns, suggesting the absence of remarkable secondary phase formation. However, minor or amorphous phases below the detection limit of XRD cannot be completely excluded.

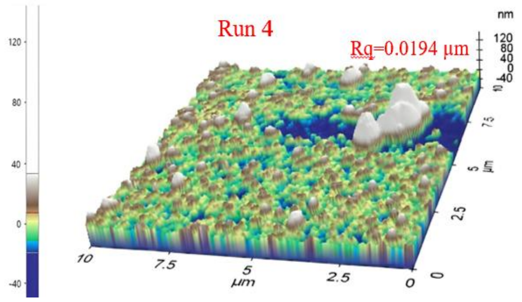

Fig. 13. AFM 3D view of the Run 4 sample.

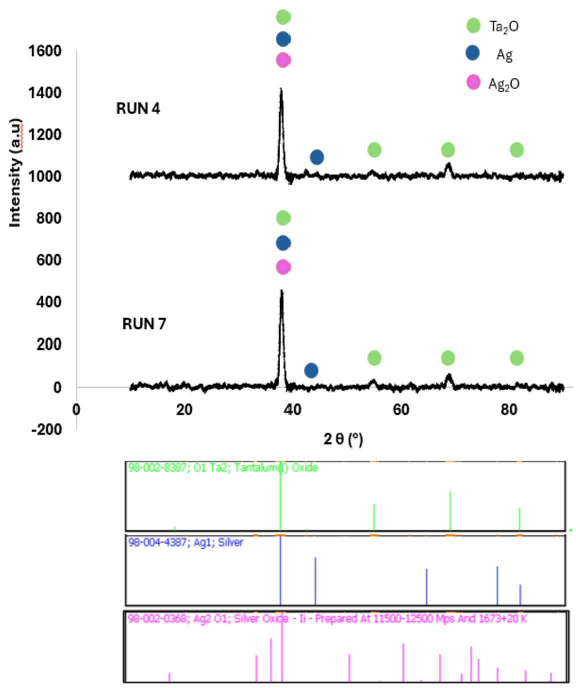

Fig.14. XRD patterns of the Run 4 and 7 samples.

3.9. CT evaluation

The indirect evaluation of CT in 13 experimental runs resulted in values ranging from 1.07 µm to 3.13 µm, revealing a significant response to the differing deposition parameters. A preliminary observation suggested that high levels of RF power (200 W) and Ag deposition time (40 min) are largely correlated with maximum thickness, as evidenced by the maximum thickness of 3.13 µm being obtained in Run 4. By contrast, the minimum thickness was acquired in Run 6, indicating that substantial changes in deposition time may contribute to the poor stability of coating growth. The comparative uniformity perceived at the centre points (Runs 9–13) reinforces the reproducibility of the scratch profiling method for estimating thickness throughout various samples.

4. Conclusions

Amongst parameters, Ag deposition time and RF power have the greatest influence on scratch distance and contact angle, and their high values promote good adhesive performance and wettability. The positive linear relationship of deposition time and RF power with adhesion strength ($R^2 = 0.9105$) indicates that long sputtering times and high energy levels lead to strong bonding. However, the interaction plot for contact angle shows an optimal condition for wettability, with the contact angle behaviour under low RF power differing from that under high RF power. This finding indicates that fine-tuning deposition parameters is crucial for optimising adhesion and surface properties in advanced coating applications. Additionally, the Run 4 sample showed a dense and uniform microstructure with homogeneously distributed coating particles; low surface roughness (Rq = 0.0194 µm); and the confirmed existence of Ta_2O, Ag and Ag_2O phases that cooperatively lead to its excellent mechanical properties. The Run 4 sample also exhibited the maximum coating thickness of 3.13 µm. The parameter settings used in Run 4 can serve as a reference for engineers developing biofunctional coatings for surgical instruments.

Acknowledgments

The authors gratefully acknowledge Universiti Sultan Zainal Abidin, Universiti Malaysia Terengganu and the University of Malaya for providing research equipment and necessary services. This study is funded by the Ministry of Higher Education under the Fundamental Research Grant Scheme (Grant No: Ref: FRGS/1/2020/ STG05/UNISZA/02/1). The authors acknowledge the help of the technical staff from all universities.

Conflict of Interest

All authors have participated in (a) conceiving and designing this study or analysing and interpretating data; (b) drafting or revising this article critically for important intellectual content; and (c) approving the final version of this paper. This manuscript has not been submitted to, nor is it under review at, another journal or other publishing venue. The authors declare that they have no known competing financial interests or personal relationships that could have appeared to influence the work reported in this paper.

References

[1] Z. Xu, M. Liu, L. Liu, G. Chen, Y. Wu, C. Yang, N. Zhao, X. Zhang, Cu-bearing stainless steel inhibits biofilm by modulating bacterial motility, Mater. Lett., 377 (2024) 137338. 10.1016/j.matlet.2024.137338

[2] M.M. Arman, R. Ramadan, A closer look at the magnetic and optical properties of ZnFe2O4/Zn0.97Ho0.03O nanocomposite for potential use as an antimicrobial, J. Aust. Ceram. Soc., 61 (2025) 649–660. 10.1007/s41779-025-01163-6

[3] N. S. Kiran, A. Chatterjee, S. Singh, C. Yashaswini, B. G. Prajapati, Biogenic metallic nanostructure coating for prevention and control of biofilm over surgical devices and food contact surfaces: a review, Regener. Eng. Transl. Med. (2026) 10.1007/s40883-025-00540-8

[4] D. Amani, G. E. Baldvinsdóttir, V. Nagy, F. Thorsteinsson, M. Másson, Eco-friendly activation of silicone surfaces and antimicrobial coating with chitosan biopolymer, Int. J. Mol. Sci. 26 (2025). 12084.10.3390/ijms262412084

[5] S. Ojha, Biofilm-associated hospital acquired infection: epidemiology, diagnosis and management – a review, Swami Vivekananda Univ. Press (2025) 63–80. 10.1038/s41586-025-08608-9

[6] A. Panwar, K.L. Yadav, Silver doped zinc oxide nanostructures with antibacterial properties against GFP-expressing antibiotic resistant Escherichia coli, Mater. Lett., 309 (2022) 131469. 10.1016/j.matlet.2021.131469

[7] D. M. Proctor, S. E. Sansom, C. Deming, S. Conlan, R. A. Blaustein, T. K. Atkins, et al., Clonal *Candida auris* and ESKAPE pathogens on the skin of residents of nursing homes, Nature 639 (2025) 1016–1023. 10.1038/s41586-025-08608-9

[8] S. Bose, D. V. Singh, T. K. Adhya, N. Acharya, *Escherichia coli*, but not *Staphylococcus aureus*, functions as a chelating agent that exhibits antifungal activity against *Candida albicans*, J. Fungi 9 (2023) 286.10.3390/jof9030286

[9] E.S. Akpan, M. Dauda, L.S. Kuburi, D.O. Obada, Bio-inspired synthesis of hydroxyapatite materials from two natural sources: A crack behavior and biological insight, J. Aust. Ceram. Soc., 59 (2023) 511–519. 10.1007/s41779-023-00837-3

[10] R. Saranya, B.A. Devi, N.M. Sundaram, Preparation of ciprofloxacin-loaded oyster shell derived hydroxyapatite composite film for biomedical applications, J. Aust. Ceram. Soc., 59 (2023). 10.1007/s41779-023-00861-3

[11] H.S. Ningsih, B.B. Aji, M.H. Wu, S.J. Shih, Development of spray dried silver-copper co-doped β-tricalcium phosphate particles, J. Aust. Ceram. Soc., (2025) 1–18. 10.1007/s41779-025-01201-3

[12] R. Alias, R. Mahmoodian, K. Genasan, K.M. Vellasamy, M.H.A. Shukor, T. Kamarul, Mechanical, antibacterial, and biocompatibility mechanism of PVD grown silver–tantalum-oxide-based nanostructured thin film on stainless steel 316L for surgical applications, Mater. Sci. Eng. C, 107 (2020) 110304. 10.1016/j.msec.2019.110304

[13] Y. Jiang, H. Geng, J. Peng, X. Ni, L. Pei, P. Ye, R. Lu, S. Yuan, Z. Bai, Y. Zhu, H. Wang, A multifunctional superhydrophobic coating with efficient anti-adhesion and synergistic antibacterial properties, Prog. Org. Coat., 186 (2024) 108028. 10.1016/j.porgcoat.2023.108028

[14] J. Song, B. Winkeljann, O. Lieleg, Biopolymer-based coatings: Promising strategies to improve the biocompatibility and functionality of materials used in biomedical engineering, Adv. Mater. Interfaces, 7 (2020) 2000850.
10.1002/admi.202000850

[15] D. Coronel-Meneses, C. Sánchez-Trasviña, I. Ratera, K. Mayolo-Deloisa, Strategies for surface coatings of implantable cardiac medical devices, Front. Bioeng. Biotechnol. 11 (2023) 1173260
10.3389/fbioe.2023.1173260

[16] D. Rogala-Wielgus, A. Zieliński, Preparation and properties of composite coatings based on carbon nanotubes for medical applications, Carbon Lett., 34 (2024) 565–601.
10.1007/s42823-023-00626-9

[17] D.C. Hu, D.H. Kuo, J.Y. Kao, C.S. Chen, C.C. Tsao, C.Y. Hsu, Fabrication of nitride films by co-sputtering of high-entropy alloys and tungsten, J. Aust. Ceram. Soc., 59 (2023) 105–115.
10.1007/s41779-022-00816-0

[18] P. P. Li, H. X. Wu, A. Dong, Ag/AgX nanostructures serving as antibacterial agents: achievements and challenges, Rare Met. 41 (2022) 519–539.
10.1007/s12598-021-01822-0

[19] L. El Fedyl, A. Nabgui, K. Agayr, M. H. V. Baouab, A. Brik, P. Thébault, et al., Biobased chitosan films incorporating rosemary-mediated silver nanoparticles for enhanced antimicrobial activity and catalytic applications, Int. J. Biol. Macromol. 349 (2026) 150850.10.
10.1016/j.ijbiomac.2026.150850

[20] T. Bruna, F. Maldonado-Bravo, P. Jara, N. Caro, Silver nanoparticles and their antibacterial applications, Int. J. Mol. Sci., 22 (2021) 7202.
10.3390/ijms22137202

[21] D. A. Narayana, M. Savanur, S. Pandey, A. Kausar, K. Gupta, Silver: the need for evaluation of nutritional and biological role, Int. J. Ayurveda Res. 7 (2026) 36–44.
10.4103/ijar.ijar_16_2

[22] Q. Hu, H. Chen, H. Cheng, J. Zhang, X. Shi, C. Gao, Biocompatible and antibacterial polymers for biomedical applications: a minireview, Biomed. Mater. 21 (2026) 012003.
10.1088/1748-605X/ae2a8c

[23] T. Phan, J. E. Jones, M. Chen, D. K. Bowles, W. P. Fay, Q. Yu, A biocompatibility study of plasma nanocoatings onto cobalt chromium L605 alloy for cardiovascular stent applications, Materials 15 (2022) 5968.
10.3390/ma15175968

[24] R. Alias, R. Mahmoodian, M.H.A. Shukor, B.S. Yew, M. Muhamad, Enhancement of as-sputtered silver-tantalum oxide thin film coating on biomaterial stainless steel by surface thermal treatment, AIP Conf. Proc., 1948 (2018) 020003. 10.1063/1.5030882

[25] R. Alias, R. Mahmoodian, M.H.A. Shukor, Effect of temperature ramp rate on the morphology, phase and adhesion strength of Ag–Ta2O5 thin film, JOM, 72 (2020) 697–705.
10.1007/s11837-019-03794-0

[26] Z. Liu, L. Huang, L. Qi, J. Wang, H. Xu, H. Yang, et al., Activating angiogenesis and immunoregulation to propel bone regeneration via deferoxamine-laden Mg-mediated tantalum oxide nanoplatform, ACS Appl. Mater. Interfaces 16 (2024) 24384–24397.10.1021/acsami.4c04316

[27] O. Auciello, Review of materials science and technological applications of transformational integrated multifunctional oxide/ultrananocrystalline diamond films/crystalline diamond, J. Mater. Res. 38 (2023) 571–585.
10.1557/s43578-023-00897-y

[28] L. Wei, Q. Huang, Y. Tu, S. Song, X. Zhang, B. Yu, et al., Plasma exosomes from patients with active thyroid-associated orbitopathy induce inflammation and fibrosis in orbital fibroblasts, J. Transl. Med. 22 (2024) 546.
10.1186/s12967-024-05263-y

[29] X. Ge, T. Li, M. Yu, H. Zhu, Q. Wang, X. Bi, et al., Strategies to reduce infection in tantalum and its derivatives applied to implants: a review, Biomed. Eng. Biomed. Tech. 68 (2023) 225–240.
10.1515/bmt-2022-0211.

[30] P. Sadhukhan, S. Banerjee, H. Kumar, A. K. Mishra, A. Banerjee, B. Maji, M. M. Ghosh, Development of orthopedic implant through computational modeling and additive manufacturing: a review, J. Mater. Eng. Perform. (2025) 1–28.
10.1007/s11665-025-11992-y.

[31] Z. Mukhtar, A. Dey, N. Kundan, F. A. Mir, Advancements in biomedical coatings: a comprehensive review of DC magnetron sputtering on Ti–6Al–4V alloy, Proc. Inst. Mech. Eng. Part J 240 (2026) 364–381.. 10.1177/13506501241282751

[32] P. Borowski, J. Myśliwiec, Recent advances in magnetron sputtering: from fundamentals to industrial applications, Coatings 15 (2025) 922. 10.3390/coatings15080922.

[33] X. Niu, G. Dong, S. Wei, Y. Wang, B. Wang, H. Tian, Effects of nitrogen flow rate on microstructure and mechanical and tribological properties of TiAlN films prepared via reactive magnetron sputtering, Ceram. Int. 49 (2023) 19885–19894. 10.1016/j.ceramint.2023.03.108

[34] W. Tang, X. Zhao, Y. Chen, B. Zhou, H. Zhang, Z. Chen, et al., High deposition rates via radio-frequency magnetron sputtering for thin electrolyte fabrication in solid oxide fuel cell applications, J. Power Sources 646 (2025) 237259. 10.1016/j.jpowsour.2025.237259

[35] R. Karthikeyan, C. T. Cherian, R. P. Fernandes, RF magnetron sputtering: a promising synthesis route for scalable production of thin-film batteries, J. Mater. Sci. 60 (2025) 8569–8601.10.1007/s10853-025-10929-z.

[36] J.Q. Liu, L.J. Li, B. Wei, F. Wen, H.T. Cao, Y.T. Pei, Effect of sputtering pressure on the surface topography, structure, wettability and tribological performance of DLC films coated on rubber by magnetron sputtering, Surf. Coat. Technol., 365 (2019) 33–40. 10.1016/j.surfcoat.2018.05.012

[37] R. Alias, R. Mahmoodian, M.H.A. Shukor, Development and characterisation of a multilayer silver/silver-tantalum oxide thin film coating on stainless steel for biomedical applications, Int. J. Adhes. Adhes., 92 (2019) 89–98. 10.1016/j.ijadhadh.2019.04.010

[38] B.W. Stuart, M. Gimeno-Fabra, J. Segal, I. Ahmed, D.M. Grant, Mechanical, structural and dissolution properties of heat treated thin-film phosphate based glasses, Appl. Surf. Sci., 416 (2017) 605–617. 10.1016/j.apsusc.2017.04.110

[39] S. Gleich, R. Soler, H. Fager, H. Bolvardi, J.O. Achenbach, M. Hans, D. Primetzhofer, J.M. Schneider, G. Dehm, C. Scheu, Modifying the nanostructure and the mechanical properties of Mo2BC hard coatings: Influence of substrate temperature during magnetron sputtering, Mater. Des., 142 (2018) 203–211. 10.1016/j.matdes.2018.01.029

[40] D. Saeed, D. Feldman, A.E. Banayosy, E. Birks, E. Blume, J. Cowger, C. Hayward, U. Jorde, J. Kremer, G. MacGowan, S. Maltais, S. Maybaum, M. Mehra, K.B. Shah, P. Mohacsi, M. Schweiger, S.E. Schroeder, P. Shah, M. Slepian, D. D'Alessandro, The 2023 International Society for Heart and Lung Transplantation Guidelines for Mechanical Circulatory Support: A 10-Year Update, J. Heart Lung Transplant., 42 (2023) e1–e222. 10.1016/j.healun.2022.12.004

[41] D. Pathote, P. Kumari, V. Singh, D. Jaiswal, R.K. Gautam, C.K. Behera, Biocompatibility evaluation, wettability, and scratch behavior of Ta-coated 316L stainless steel by DC magnetron sputtering for orthopedic applications, Surf. Coat. Technol., 459 (2023) 29392. 10.1016/j.surfcoat.2023.129392

[42] W. Tillmann, J. Urbanczyk, A. Thewes, G. Braeuer, N.F.L. Dias, Effect of the TiSiN interlayer properties on the adhesion and mechanical properties of multilayered TiSiCN thin films, Surf. Coat. Technol., 478 (2024) 130467. 10.1016/j.surfcoat.2024.130467

[43] W. Liu, Z. Xu, J. Peng, C. Wang, Microwave plasma etching of SS304 substrates for improved PVD coating adhesion, Appl. Surf. Sci., 708 (2025) 163738. 10.1016/j.apsusc.2025.163738

[44] S. Zhu, Y. Xu, R. Liu, Y. Yu, X. Duan, Y. Lei, … J. Tang, Preparation of high-temperature antioxidant coatings on tantalum-based surfaces by atmospheric plasma spraying and their microstructural characterisation, Surf. Coat. Technol., 501 (2025) 131928. 10.1016/j.surfcoat.2025.131928

التحليل الإحصائي لمعلمات الترسيب للأغشية الرقيقة متعددة الطبقات من AgO/Ag–TaO/TaO على ركيزة من الفولاذ المقاوم للصدأ SS316L

Mohd Amirul [1], Rodianah Alias [1,2]*, Muhammad Rizwan [3], W.N.F Mohamad [4], Abd Rahman Z. [5], M. S. Hamid [6], Afifah Juri [7], Mohd Faizal Ali Akhbar [8] and Abd Razak Bushroa [9]

[1,4,5,6] *Faculty of Innovative Design and Technology, Universiti Sultan Zainal Abidin, Campus Gong Badak, 21300 Kuala Nerus, Terengganu Darul Iman, Malaysia*

[1]*Faculty of Information Sciences and Engineering, Management and Science University, University Drive, Off Persiaran Olahraga, Section 13, 40100 Shah Alam, Selangor, Malaysia*

[2] *Biomaterials & Nanomaterials Research Group, Smart Technology Cluster, Faculty of Innovative Design and Technology, Universiti Sultan Zainal Abidin, Campus Gong Badak, 21300 Kuala Nerus, Terengganu Darul Iman, Malaysia*

[3] *Department of Metallurgical Engineering, Faculty of Chemical and Process Engineering, NED University of Engineering and Technology, 75270, Karachi, Pakistan*

[7] *Department of Mechanical and Manufacturing Engineering, Faculty of Engineering and Built Environment, Universiti Kebangsaan Malaysia, 43600 Bangi, Selangor, Malaysia*

[8] *Department of Naval Architecture and Maritime Technology, Faculty of Ocean Engineering Technology, Universiti Malaysia Terengganu, 21030 Kuala Nerus, Terengganu, Malaysia*

[9] *Department of Mechanical Engineering, Faculty of Engineering, Universiti Malaya, 50603 Kuala Lumpur, Malaysia*

* Corresponding author: rodianahalias@unisza.edu.my

المستخلص

تتطلب الأدوات الجراحية المصممة لتحقيق أداء عالٍ طلاءات تتمتع بخصائص ميكانيكية قوية، وخصائص مقاومة للماء، وتوافقًا مع الأنسجة البيولوجية لتقليل التفاعلات مع سوائل الجسم إلى أدنى حد ممكن أثناء الجراحة. في هذه الدراسة، تم التحقيق في الخصائص الهيكلية والسطحية للأغشية الرقيقة متعددة الطبقات من AgO/Ag–TaO/TaO المودعة على ركيزة من الفولاذ المقاوم للصدأ ٣١٦L (SS316L) عن طريق الترسيب الفيزيائي للبخار باستخدام تقنية الرش المغناطري، كدالة لمعلمات الترسيب المختلفة. وقد تمت دراسة تأثير مدة ترسيب AgO وقوة الرش بالترددات الراديوية (RF) باستخدام تصميم مركب مركزي مع منهجية سطح الاستجابة. وأظهرت النتائج وجود ارتباط كبير بين القيم المتوقعة والقيم الفعلية لقوة الالتصاق ($R^2 = 0.9105$)، مما يؤكد ملاءمة النموذج. وتأثرت قوة الالتصاق بشكل كبير بقوة الرش بالترددات الراديوية، ثم بمدة الترسيب. كما تأثرت قابلية التبلل بهذه المعلمات. تُظهر مخططات التفاعل تحسّنًا في قابلية التبلل عند مستويات معينة من طاقة التردد اللاسلكي، مع زاوية تلامس قصوى تبلغ ٨٩,٦°. تم الحصول على قوة الالتصاق المثلى في ظل ظروف محددة لطاقة التردد اللاسلكي ووقت الترسيب، مع مسافة خدش قصوى تبلغ ٧٠٥ ميلينيوتن. يقدم هذا العمل رؤى مفيدة حول دور معلمات الترسيب في تكييف أداء الأغشية الرقيقة للتطبيقات الطبية الحيوية والصناعية.